

₁ Study of the multi-strange resonance $\Xi(1530)^0$ production
₂ with ALICE at the LHC energies

₃ Jihye Song

4 Contents

5	List of Figures	4
6	List of Tables	6
7	1 The physics of relativistic heavy-ion collisions	7
8	1.1 Standard model	7
9	1.2 Quantum Chromo-Dynamics	7
10	1.3 Heavy Ion Collisions	7
11	2 Production of resonance with strangeness	7
12	2.1 Resonance with strangeness	7
13	3 Theoretical models	7
14	3.1 Thermal statistical model	7
15	3.1.1 Calculations	9
16	3.1.2 Results	9
17	3.1.3 Comparison with data	11
18	3.2 UrQMD	11
19	4 A Large Ion Collider Experiment at the LHC	11
20	4.1 The Large Hadron Collider	12
21	4.2 The ALICE project	12
22	4.2.1 ALICE detector	12
23	4.2.2 Data Acquisition (DAQ) and trigger system	12
24	4.2.3 ALICE offline software frame work	12
25	5 Measurement of $\Xi(1530)^0$ production in p–Pb	12
26	5.1 $\Xi(1530)^0$ -reconstruction	13
27	5.1.1 Data sample and event selection	13
28	5.1.2 Track and topological selection	16
29	5.1.3 Particle identification	17
30	5.1.4 Signal extraction	20
31	5.2 Efficiency correction	24
32	5.3 Corrected p_T -spectra	26
33	5.4 Systematic uncertainties	27
34	5.4.1 Subgroup of systematic uncertainties	28
35	5.4.2 Summary of systematic uncertainties	30
36	5.5 $\Xi(1530)^0$ transverse momentum spectra	33

37	6	Measurement of $\Xi(1530)^0$ production in Pb–Pb	33
38	6.1	$\Xi(1530)^0$ -reconstruction	34
39	6.1.1	Data sample and event selection	34
40	6.1.2	Topological selection	35
41	6.1.3	Particle identification	35
42	6.2	Efficiency correction	35
43	6.3	Systematic uncertainties	35
44	6.4	$\Xi(1530)^0$ transverse momentum spectra	35
45	7	Results	35
46	7.1	dN/dy and $\langle p_T \rangle$	35
47	7.2	Particle yield ratios	35
48	7.2.1	Comparison with other resonances	35
49	7.2.2	Comparison with models	35
50	References		35

51 **List of Figures**

52 1	Ratio of baryonic and mesonic resonances over their stable partner as a function of temperature.	10
54 2	Ratio of resonances over their stable partner as a function of $\sqrt(s)$	11
55 3	Vertex-z coordinate distribution of the accepted events in full multiplicity range 0-100%. The red dashed line indicates vertex cut	14
57 4	Multiplicity distribution of accepted events in percentile. The each color and labels define the four intervals in which the analysis is performed.	15
59 5	Sketch of the decay modes for Ξ^{*0} (right) and depiction of the track and topological selection criteria.	17
61 6	TPC dE/dx as function of transverse momentum for total (top) and selected first emitted π in 3σ (bottom)	18
63 7	TPC dE/dx as function of transverse momentum for total (top) and selected second emitted π in 3σ (bottom)	18
65 8	TPC dE/dx as function of transverse momentum for total (top) and selected last emitted π in 3σ (bottom)	19
67 9	TPC dE/dx as function of transverse momentum for total (top) and selected proton in 3σ (bottom)	19
69 10	The $\Xi^\mp\pi^\pm$ invariant mass distribution (Same-event pairs) in $1.8 < p_T < 2.2 \text{ GeV}/c$ and for the multiplicity class 20-40%. The background shape, using pairs from different events (Mixed-event background), is normalised to the counts in $1.49 < M_{\Xi\pi} < 1.51 \text{ GeV}/c^2$ and $1.56 < M_{\Xi\pi} < 1.58 \text{ GeV}/c^2$	20
71 11	The invariant mass distribution after subtraction of the mixed-event background. The solid curve represents the combined fit, while the dashed line describes the residual background.	21
73 12	σ fit parameters as a function of p_T in MB.	22
75 13	$\Xi(1530)^0$ -mass obtained from fit of the Voigtian peak as a function of p_T in each multiplicity classes.	23
77 14	$\Xi(1530)^0$ -raw spectra obtained from fit of the Voigtian peak and a polynomial residual background for different multiplicities. Only the statistical error is reported.	23
79 15	$\Xi(1530)^0$ -raw spectra obtained from fit of the Voigtian peak and a polynomial residual background for different multiplicities. Only the statistical error is reported.	24
81 16	Real corrected $\Xi(1530)^0$ spectrum (black) for the minimum bias with Levy fit (black curve). Also shown are the unweighted generated (blue) and reconstructed (red) $\Xi(1530)^0$ spectra.	25
83 17	$\Xi(1530)^0$ -raw spectra obtained from fit of the Voigtian peak and a polynomial residual background for different multiplicities. Only the statistical error is reported.	26

91	18	Corrected p_T -spectra of $\Xi(1530)^0$ in NSD and different multiplicity classes.	27
92	19	Summary of the contributions to the systematic uncertainty after consistency check in MB. The dashed black line is the sum in quadrature of all the contributions.	30
93			
94	20	Summary of the contributions to the systematic uncertainty after consistency check for each multiplicity class(0-20-40-60-100). The dashed black line is the sum in quadrature of all the contributions.	31
95			
96	21	Fractional systematic uncertainties for each multiplicity classes.	31
97			
98	22	Fractional smoothed systematic uncertainties for each multiplicity classes.	32
99			
100	23	Corrected yields as function of p_T in NSD events and multiplicity dependent event classes. Statistical and systematical uncertainties are plotted separately.	33
101			

¹⁰² **List of Tables**

¹⁰³	1	Parameters used in the thermal-model calculations.	8
¹⁰⁴	2	Properties of particles used in the ratio calculations.	9
¹⁰⁵	3	Difference of mass (ΔM), baryon number (ΔB), strangeness (ΔS) and charge (ΔQ) of the ratios. The values of the slopes needs to be checked!!!! .	11
¹⁰⁶	4	Number of events at different selection stages.	15
¹⁰⁷	5	Number of accepted and analysed events per multicity interval	15
¹⁰⁸	6	Track selections common to all decay daughters and primary track selections applied to the charged pions from decays of Ξ^{*0}	16
¹⁰⁹	7	Topological and track selection criteria.	17
¹¹⁰	8	Alternate sets of topological parameters in the analysis.	29
¹¹¹			
¹¹²			

113 **1 The physics of relativistic heavy-ion collisions**

114 This test for references [1]

115 **1.1 Standard model**

116 **1.2 Quantum Chromo-Dynamics**

117 **1.3 Heavy Ion Collisions**

118 **2 Production of resonance with strangeness**

119 **2.1 Resonance with strangeness**

120 **3 Theoretical models**

121 **3.1 Thermal statistical model**

122 The statistical-thermal model has proved extremely successful in applications to relativistic
123 collisions of both heavy ions and elementary particles. In light of this success, THERMUS,
124 a thermal model analysis package, has been developed for incorporation into the object-
125 oriented ROOT framework [2].

126
127 There are three types of statistical-thermal models in explaining data in high energy nu-
128 clear physics and THERMUS treats the system quantum numbers B (baryon number), S
129 (strangeness) and Q (charge) within three distinct formalisms:

130 1. **Grand-Canonical Ensemble:** Because the hot dense matter produced in nucleus-
131 nucleus collisions is large enough, this ensemble is the most widely used in applications
132 to heavy-ion collisions, in which the quantum numbers are conserved on average.

133 2. **Fully-Canonical Ensemble:** In which B, S and Q are each exactly conserved and
134 this ensemble used in high-energy elementary collisions such as pp, p \bar{p} and e $^-$ e $^+$
135 collisions.

136 3. **Strangeness-Canonical Ensemble:** In small systems or at low temperatures, a
137 canonical treatment leads to a suppression of hadrons carrying non-zero quantum
138 numbers, since these particles have to be created in pairs and the resulting low
139 production of strange particles requires a canonical treatment of strangeness.

140 In order to calculate the thermal properties of a system, one starts with an evaluation
141 of its partition function. The form of the partition function obviously depends on the
142 choice of ensemble. In the present analysis the strangeness-canonical ensemble used and
143 the statistical-thermal model requires six parameters as input: the chemical freeze-out

¹⁴⁴ temperature T , baryon and charge chemical potentials μ_B and μ_Q respectively, canonical
¹⁴⁵ or correlation radius, R_C ; the radius inside which strangeness is exactly conserved and the
¹⁴⁶ fireball radius R . An additional strangeness saturation factor γ_S has been used as indicator
¹⁴⁷ of a possible departure from equilibrium and $\gamma_S = 1.0$ corresponds to complete strangeness
¹⁴⁸ equilibration.

¹⁴⁹ The volume dependence cancels out when studying the particle ratios as well as strangeness
¹⁵⁰ canonical equivalent to grand canonical formalism if $\Delta S = 0$ in the ratios and γ_S also can-
¹⁵¹ cels out. Parameters used in the analysis listed in Table 1. The μ_B parameter taken from
¹⁵² the Ref. [3].

Table 1: Parameters used in the thermal-model calculations.

Parameter	Value
T (MeV)	varied (see text)
μ_B (MeV)	$9.2 \times 10^{-2}????$
μ_Q (MeV)	0.0
γ_S	1.0

154 **3.1.1 Calculations**

155 *Concept:*

156 In order to calculate the particle ratios within strangeness canonical formalism of THER-
157 MUS, temperature varied between 60 MeV to 180 MeV and particle yields extracted for
158 each temperature value and then primary particle ratios calculated for each case.

159

160 *Feed-Down Correction:*

161 Since the particle yields measured by the detectors in collision experiments include feed-
162 down from heavier hadrons and hadronic resonances, the primordial hadrons are allowed to
163 decay to particles considered stable by the experiment before model predictions are com-
164 compared with experimental data. In the analysis only Λ particles counted as stable (do not
165 allowed to decay) so there is no feed-down contribution from these particles to the other
166 ratios.

167

168

169 Properties of studied particles and their particle ratios listed in Table 2 and Table 3,
170 respectively.

Table 2: Properties of particles used in the ratio calculations.

Particle	Δ^{++}	p	K^{*0}	K^0	K^+	Λ^*	Λ	Σ^{*+}	Σ^+	Σ^0
Mass (MeV/c^2)	1232	938.27	895.92	497.61	493.67	1519.5	1115.68	1382.8	1189.37	1192.6
Width (MeV/c^2)	120	–	50.7	–	–	15.6	–	37.6	–	–
$c\tau$ (fm)	1.6	–	3.9	–	–	12.6	–	5.51	–	–
Ang. Momentum (J)	3/2	1/2	1	1	0	3/2	1/2	3/2	1/2	1/2
Isospin (I)	3/2	1/2	1/2	1/2	1/2	0	0	1	1	1
Parity (P)	+1	+1	-1	-1	0	-1	+1	+1	+1	+1
Strangeness (S)	0	0	1	1	1	-1	-1	-1	-1	-1
Baryon Number (B)	1	1	0	0	0	1	1	1	1	1
Decay Channel	$p\pi^+$	–	π^-	–	$\mu^+\nu_\mu$	pK^-	$p\pi^-$	$\Lambda\pi^+$	$p\pi^0$	$\Lambda\gamma$
Branching Ratio (%)	~ 100	–	~ 66.7	–	~ 63.54	~ 45	~ 63.9	~ 87	~ 51.6	~ 100
Q-Value(MeV/c^2)	154.16	–	262.68	–	–	87.55	37.84	127.55	111.53	76.96

171

172

173 **3.1.2 Results**

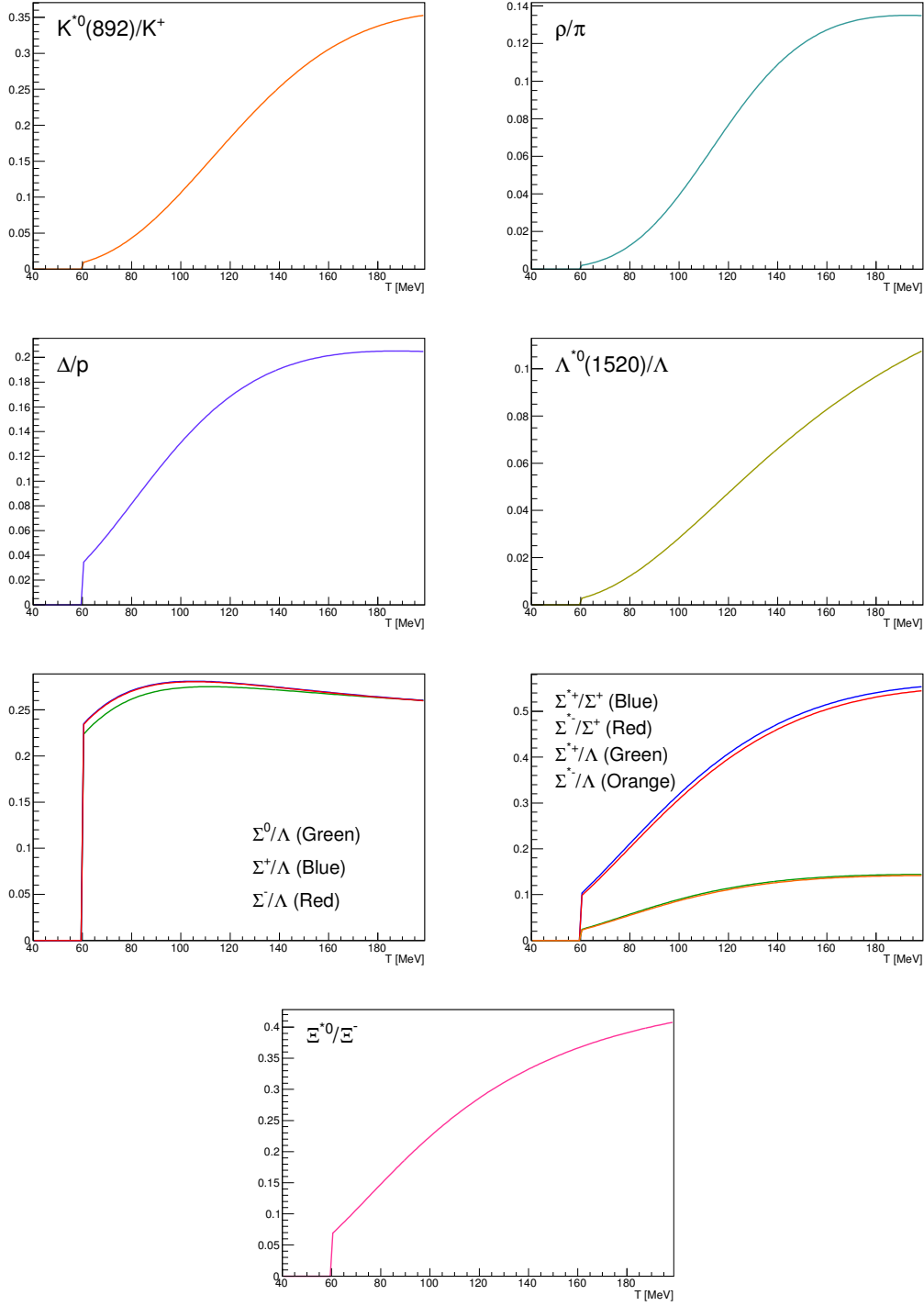


Figure 1: Ratio of baryonic and mesonic resonances over their stable partner as a function of temperature.

Table 3: Difference of mass (ΔM), baryon number (ΔB), strangeness (ΔS) and charge (ΔQ) of the ratios. The values of the slopes needs to be checked!!!!

Particle	Δ^{++}/p	K^*/K^+	Λ^*/Λ	Σ^{*+}/Λ	Σ^{*+}/Σ^0	Σ^0/Λ	Σ^{*+}/Σ^+	Ξ^{*0}/Ξ^-
ΔM (MeV/ c^2)	293.8	402.25	403.82	267.12	190.16	76.96	193.43	210.49
ΔB	0	0	0	0	0	0	0	0
ΔS	0	0	0	0	0	0	0	0
ΔQ	+1	-1	0	+1	0	+1	0	-1
Slope (%) per MeV ????????	0.19	0.76	0.98	0.25	-	-0.08	0.37	0.42

174 3.1.3 Comparison with data

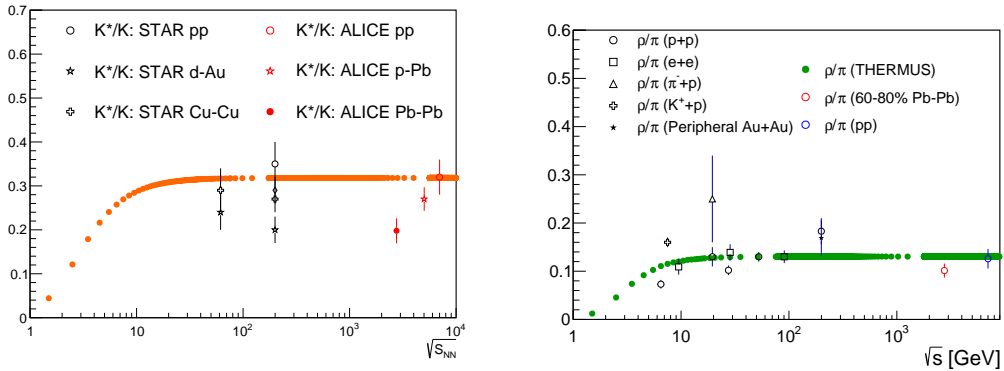


Figure 2: Ratio of resonances over their stable partner as a function of $\sqrt{(s)}$.

175 3.2 UrQMD

176 4 A Large Ion Collider Experiment at the LHC

177 ALICE (A Large Ion Collider Experiment) has been collecting data during the whole first
 178 phase of the Large Hadron Collider operations, from its startup on the 23 November 2009
 179 to the beginning of the first long technical shutdown in February 2013. During the first
 180 three years of operations LHC provided pp collisions at 0.9, 2.76, 7 and 8 TeV, Pb?Pb
 181 collisions at 2.76A TeV and finally p?Pb collisions at 5.02 TeV. The first section of this
 182 chapter focuses on the LHC performance during this phase and includes details on the
 183 accelerator parameters that allow the LHC to perform as a lead ion collider. A detailed
 184 description of the ALICE detector follows in the section 2.2. ALICE has been designed and

185 optimized to study the high particle-multiplicity environment of ultra-relativistic heavy-ion
186 collisions and its tracking and particle identification performance in Pb-Pb collisions are
187 discussed. The attention is drawn in particular on the central barrel detectors. Section
188 2.3 describes the ALICE Data Acquisition (DAQ) system, that also embeds tools for the
189 online Data Quality Monitoring (DQM). The final part of the chapter is dedicated to the
190 offline computing and reconstruction system based on the GRID framework.

191 4.1 The Large Hadron Collider

192 The Large Hadron Collider (LHC) [57], [58] is a two-ring-superconducting hadron acceler-
193 ator and collider installed in the 26.7 Km tunnel that hosted the LEP ma- chine and it
194 completes the CERN accelerator complex together with the PS and SPS, among the others
195 shown in fig. 2.1. Four main experiments are located in four different interaction points
196 along its circumference. ATLAS and CMS, the biggest ones, are multi-purpose detectors
197 built to discover the Higgs boson and hints of new physics beyond the Standard Model.
198 LHCb is dedicated to the physics of the flavour, focusing on the study CP-violation using B
199 meson decay channels. The phenomena that these three experiments aim to observe have
200 production cross sec- tion of the order of a hundred of pb or lower, therefore a large number
201 of collision events is required to the machine in order to fulfill the LHC pp physics program.
202 ALICE, on the contrary, is dedicated to the physics of Quark Gluon Plasma through the
203 observation of high-energy heavy-ion collisions, although a shorter physics pro- gram with
204 pp collisions has been carried out.

205 4.2 The ALICE project

206 4.2.1 ALICE detector

207 4.2.2 Data Acquisition (DAQ) and trigger system

208 4.2.3 ALICE offline software frame work

209 5 Measurement of $\Xi(1530)^0$ production in p–Pb

210 The measurement of resonance production in p–Pb collisions helps to disentangle cold
211 nuclear matter effects from genuine hot medium effects and contribute to the study of
212 the system size dependence of re-scattering in the hadronic phase. In order to study the
213 particle production mechanism, the $\Xi(1530)^0$ resonance production at mid-rapidity ($-0.5 <$
214 $y_{\text{CMS}} < 0$) is measured in p–Pb collisions $\sqrt{s_{\text{NN}}} = 5.02$ TeV with the ALICE experiment,
215 via the reconstruction of its hadronic decay into $\Xi\pi$.

216 **5.1 $\Xi(1530)^0$ -reconstruction**

217 The Ξ^* production in p–Pb collisions at $\sqrt{s_{\text{NN}}} = 5.02$ TeV at mid-rapidity has been studied
218 in different multiplicity classes, from very central to peripheral collisions. The analysis
219 strategy is based on the invariant mass study of the reconstructed pairs (referred to as
220 the candidates) whose provenance could be the decay of a Ξ^* baryon into charged parti-
221 cles. The decay products (also called daughters in the text) are identified as oppositely
222 charged Ξ and π among the tracks reconstructed in the central barrel. The event selection,
223 track selection and the particle identification strategy is described. The raw signal yield
224 is extracted by fitting the background-subtracted invariant mass distribution in several
225 transverse momentum intervals. In order to extract the p_{T} -dependent cross section, these
226 yields are corrected for efficiency. The p_{T} -dependent correction due to the detector ac-
227 ceptance and reconstruction efficiency, $(\text{Acc} \times \epsilon_{\text{rec}})(p_{\text{T}})$, is computed from a Monte Carlo
228 simulation. The absolute normalisation is then performed, by dividing for the number of
229 the events in each multiplicity classes.

230 **5.1.1 Data sample and event selection**

231 A description of the ALICE detector and of its performance during the LHC Run 1 (2010–
232 2013) can be found in [4, 5]. The data sample was recorded during the LHC p–Pb run
233 at $\sqrt{s_{\text{NN}}} = 5.02$ TeV in 2013. Due to the asymmetric energies of the proton (4 TeV) and
234 lead ion (1.57 A TeV) beams, the centre-of-mass system in the nucleon-nucleon frame is
235 shifted in rapidity by $\Delta y_{\text{NN}} = 0.465$ towards the direction of the proton beam with respect
236 to the laboratory frame of the ALICE detector [6]. For the analysed p–Pb data set, the
237 direction of the proton beam was towards the ALICE muon spectrometer, the so-called “C”
238 side, standing for negative rapidities; conversely, the Pb beam circulated towards positive
239 rapidities, labelled as “A” side in the following. The analysis in this paper was carried out
240 at midrapidity, in the rapidity window $-0.5 < y_{\text{CMS}} < 0$.

241 The minimum-bias trigger during the p–Pb run was configured to select events by
242 requiring a logical OR of signals in V0A and V0C [5], two arrays of 32 scintillator detectors
243 covering the full azimuthal angle in the pseudo-rapidity regions $2.8 < \eta_{\text{lab}} < 5.1$ and
244 $-3.7 < \eta_{\text{lab}} < -1.7$, respectively [7]. In the data analysis it was required to have a
245 coincidence of signals in both V0A and V0C in order to reduce the contamination from
246 single-diffractive and electromagnetic interactions. This left only Non-Single Diffractive
247 (NSD) events, which amount for a total of 109.3 million events, in the Minimum-Bias
248 sample(~ 111.1 million events) corresponding to an integrated luminosity of about 50
249 μb^{-1} . Out of this sample, 93.9×10^6 events satisfy the following selection criteria and have
250 been actually used for the analysis:

- 251 • Events with z-coordinate of primary vertex (V_z) falling within ± 10 cm from the
252 interaction point
- 253 • Rejection of pile-up event

- 254 • Requiring primary tracks to have at least one hit in one of the two innermost layers
 255 of the ITS (silicon pixel detector, SPD)
 256 • multiplicity ranges in percentile (V0A): 0-20%, 20-40%, 40-60%, 60-100% and MB

257 The distribution of the vertex z position of the accepted events is reported in fig. 3.
 258 Events with $|V_z| < 10$ cm have been used to ensure a uniform acceptance in the central
 259 pseudo-rapidity region, $|\eta| < 0.8$, where the analysis is performed. This cut reduces the
 260 total number of events to 97.5×10^6 , that is the $\sim 87.8\%$ of the initial sample. The number
 261 of events before and after the each event selection stages are written in Table 4. Fig. 4
 262 shows the multiplicity distribution of the accepted events divided in bins of percentile.
 263 The each colours on the histogram indicate the multiplicity ranges used in this analysis.
 264 Corresponding events for each multiplicity range are in Table 5.

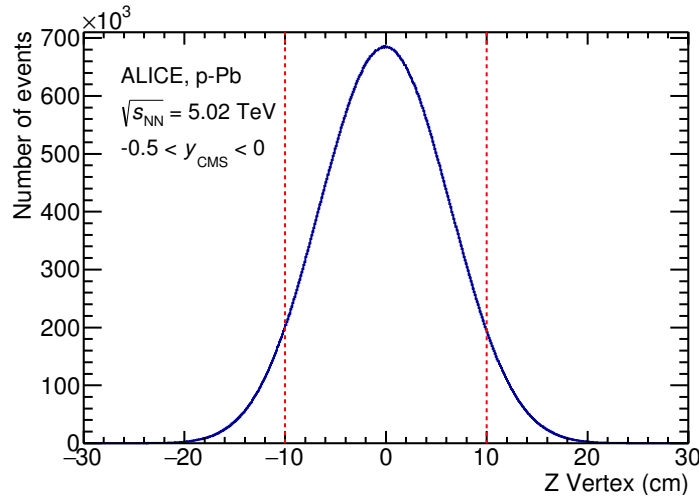


Figure 3: Vertex-z coordinate distribution of the accepted events in full multiplicity range 0-100%. The red dashed line indicates vertex cut

Event selection stage	number of events	percentage
Original number of events	111.1×10^6	100.0%
Number of triggered events (kINT7)	109.3×10^6	98.4%
Events after PV position cut ($ V_z < 10$ cm)	97.5×10^6	87.8%
Events after reject pile-up	94.5×10^6	85.1%
Events after number of SPD cluster cut (≥ 1)	93.9×10^6	84.5%

Table 4: Number of events at different selection stages.

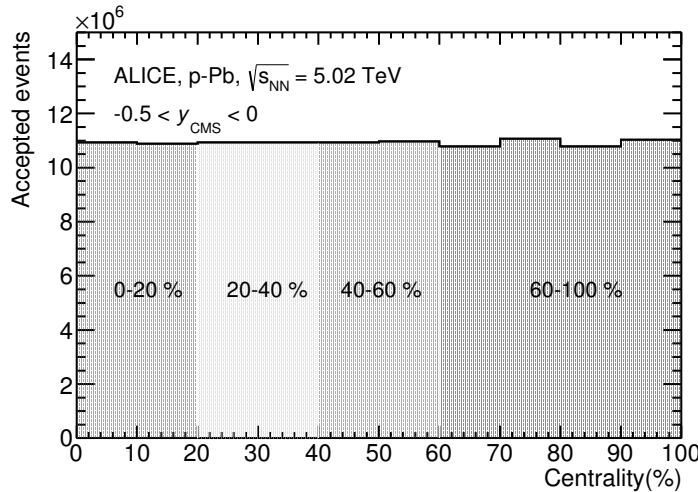


Figure 4: Multiplicity distribution of accepted events in percentile. The each color and labels define the four intervals in which the analysis is performed.

multiplicity	number of events
0-20%	21.82×10^6
20-40%	21.86×10^6
40-60%	21.91×10^6
60-100%	43.68×10^6

Table 5: Number of accepted and analysed events per multicity interval

265 **5.1.2 Track and topological selection**

266 In comparison with the Ξ^{*0} analysis carried out in pp collisions at $\sqrt{s} = 7$ TeV [8], track
 267 and topological selections were revised and adapted to the p-Pb dataset. Pions from strong
 268 decays of Ξ^{*0} were selected according to the criteria for primary tracks. As summarized in
 269 Table 6, all charged tracks were selected with $p_T > 0.15$ GeV/c and $|\eta_{\text{lab}}| < 0.8$, as described
 270 in Ref. [5]. The primary tracks were chosen with the Distance of Closest Approach (DCA)
 271 to PV of less than 2 cm along the longitudinal direction (DCA_z) and lower than $7\sigma_r$ in
 272 the transverse plane (DCA_r), where σ_r is the resolution of DCA_r . The σ_r is strongly
 273 p_T -dependent and lower than 100 μm for $p_T > 0.5$ GeV/c [5]. To ensure a good track
 274 reconstruction quality, candidate tracks were required to have at least one hit in one of the
 275 two innermost layers (SPD) of the ITS and to have at least 70 reconstructed points in the
 276 Time Projection Chamber (TPC), out of a maximum of 159. The Particle IDentification
 277 (PID) criteria for all decay daughters are based on the requirement that the specific energy
 278 loss (dE/dx) is measured in the TPC within three standard deviations (σ_{TPC}) from the
 expected value (dE/dx_{exp}), computed using a Bethe-Bloch parametrization [5].

Common track selections	$ \eta_{\text{lab}} $	< 0.8
	p_T	> 0.15 GeV/c
	PID $ (\text{d}E/\text{d}x) - (\text{d}E/\text{d}x)_{\text{exp}} $	< 3 σ_{TPC}
Primary track selections	DCA_z to PV	< 2 cm
	DCA_r to PV	< $7\sigma_r$ (p_T)
	number of SPD points	≥ 1
	number of TPC points	> 70
	χ^2 per cluster	< 4

Table 6: Track selections common to all decay daughters and primary track selections applied to the charged pions from decays of Ξ^{*0} .

279 Since pions and protons from weak decay of Λ ($c\tau = 7.89$ cm [9]) and pions from weak
 280 decay of Ξ^- ($c\tau = 4.91$ cm [9]) are produced away from the PV, specific topological and
 281 track selection criteria, as summarized in Table 7, were applied [10, 8, 11].

283 In the analysis of Ξ^{*0} , Λ and π from Ξ^- were selected with a DCA of less than 1.9 cm
 284 and with a DCA_r to the PV greater than 0.015 cm. The Λ daughter particles (π and p)
 285 were required to have a DCA_r to the PV greater than 0.06 cm, while the DCA between the
 286 two particles was required to be less than 1.4 cm. Cuts on the invariant mass, the cosine
 287 of the pointing angle ($\theta_\Lambda, \theta_\Xi$) and the radius of the fiducial volume ($r(\Lambda), r(\Xi)$) in Table 7
 288 were applied to optimize the balance of purity and efficiency of each particle sample.

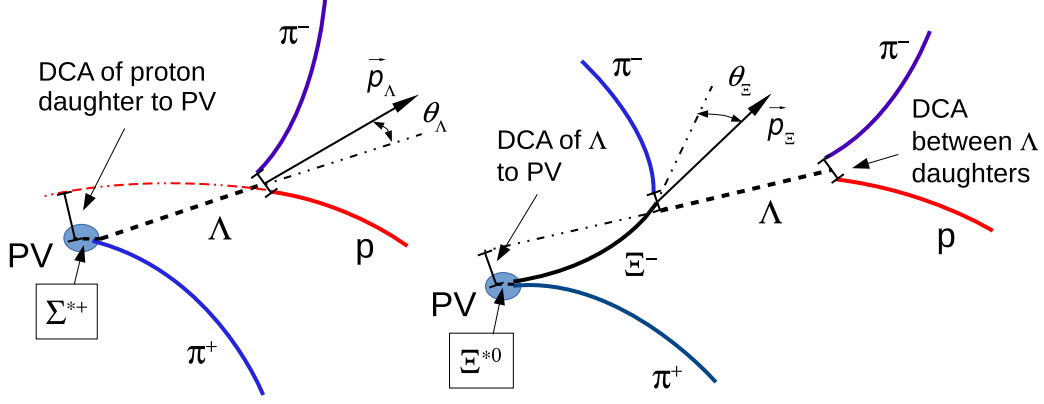


Figure 5: Sketch of the decay modes for Ξ^{*0} (right) and depiction of the track and topological selection criteria.

Topological cuts	Ξ^{*0}
DCA _r of Λ decay products to PV	> 0.06 cm
DCA between Λ decay products	< 1.4 cm
DCA of Λ to PV	> 0.015 cm
$\cos\theta_\Lambda$	> 0.875
$r(\Lambda)$	$0.2 < r(\Lambda) < 100$ cm
$ M_{p\pi} - m_\Lambda $	< 7 MeV/ c^2
DCA _r of pion (from Ξ^-) to PV	> 0.015 cm
DCA between Ξ^- decay products	< 1.9 cm
$\cos\theta_\Xi$	> 0.981
$r(\Xi^-)$	$0.2 < r(\Xi^-) < 100$ cm
$ M_{\Lambda\pi} - m_\Xi $	< 7 MeV/ c^2

Table 7: Topological and track selection criteria.

289 **5.1.3 Particle identification**

290 PID selection criteria are applied for

- 291 1. π^\pm (last emitted π) and proton from Λ

- 292 2. π^\pm (second emitted π) from Ξ^\pm
 293 3. π^\pm (first emitted π) from $\Xi(1530)^0$

294 by using TPC. On TPC dE/dx versus momentum distribution, 3σ cuts are applied to TPC
 295 for selecting each of the particles. The TPC dE/dx selection allows to have better signal
 296 with $\sim 20\%$ increase of significance.

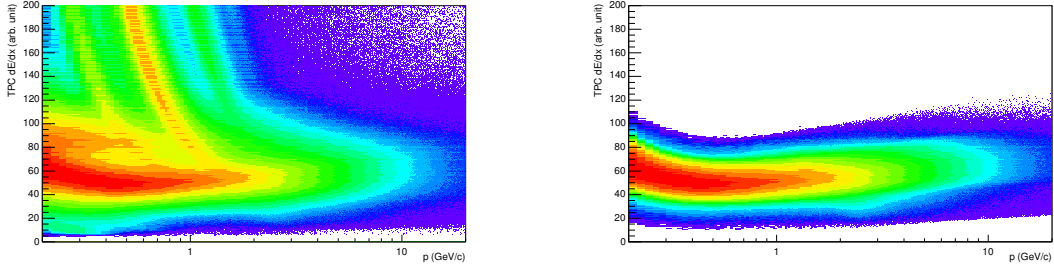


Figure 6: TPC dE/dx as function of transverse momentum for total (top) and selected first emitted π in 3σ (bottom)

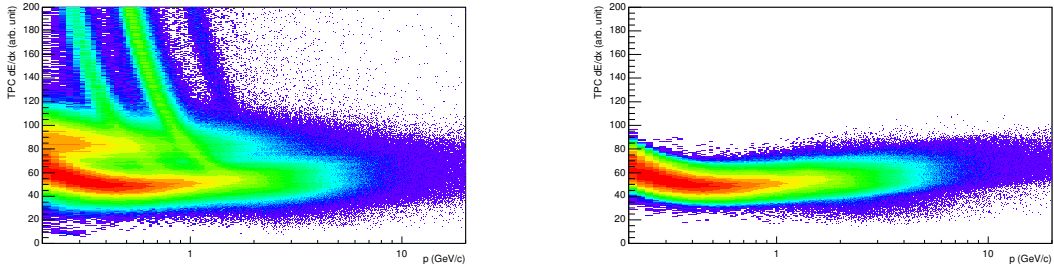


Figure 7: TPC dE/dx as function of transverse momentum for total (top) and selected second emitted π in 3σ (bottom)

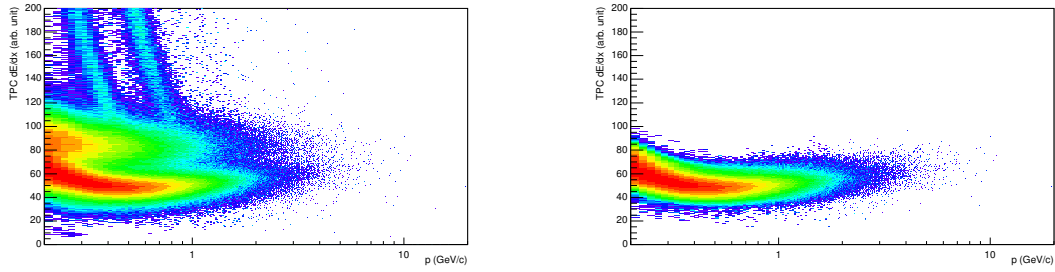


Figure 8: TPC dE/dx as function of transverse momentum for total (top) and selected last emitted π in 3σ (bottom)

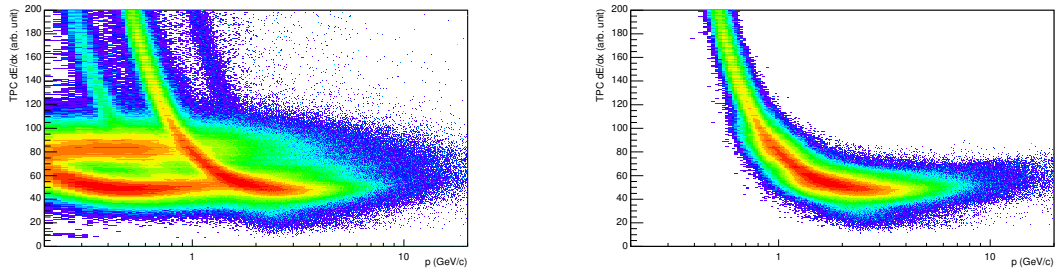


Figure 9: TPC dE/dx as function of transverse momentum for total (top) and selected proton in 3σ (bottom)

297 **5.1.4 Signal extraction**

298 The Ξ^{*0} signals were reconstructed by invariant-mass analysis of candidates for the decay
 299 products in each transverse momentum interval of the resonance particle, and for each
 300 multiplicity class. The $\Xi^-\pi^+(\Xi^+\pi^-)$ invariant mass distribution is reported in Figure
 301 5.1.4 for semi-central events (20-40%) and resonance in the range $1.8 < p_T < 2.2 \text{ GeV}/c$.

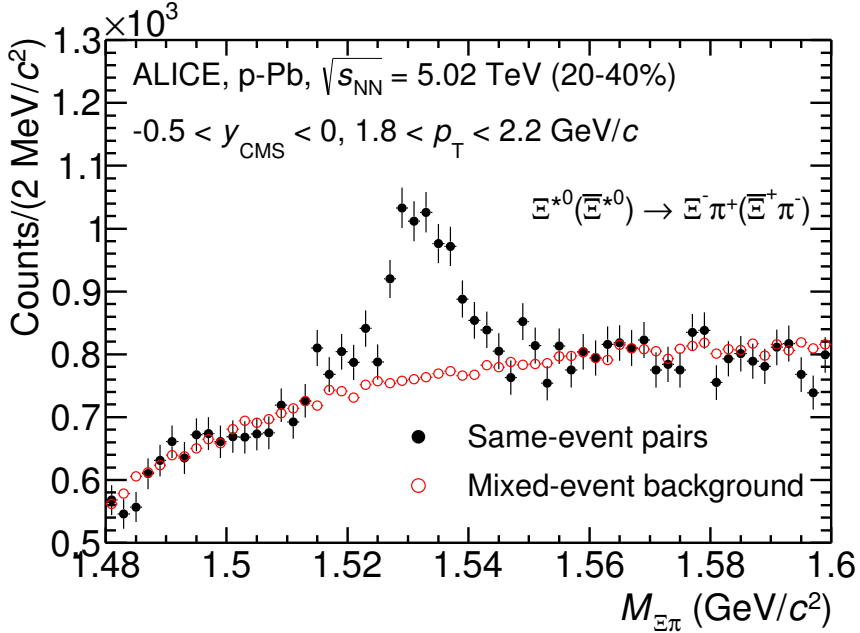


Figure 10: The $\Xi^\mp\pi^\pm$ invariant mass distribution (Same-event pairs) in $1.8 < p_T < 2.2 \text{ GeV}/c$ and for the multiplicity class 20-40%. The background shape, using pairs from different events (Mixed-event background), is normalised to the counts in $1.49 < M_{\Xi\pi} < 1.51 \text{ GeV}/c^2$ and $1.56 < M_{\Xi\pi} < 1.58 \text{ GeV}/c^2$.

302 Since the resonance decay products originate from a position which is indistinguishable
 303 from the PV, a significant combinatorial background is present. In order to extract
 304 $\Xi(1530)^0$ signal it is necessary to remove or, at least reduce, the combinatorial background.
 305 For this analysis, this has been done with the event mixing (EM) technique, by combining
 306 uncorrelated decay products 20 different events. The events for the mixing have been
 307 selected by applying the similarity criteria to minimise distortions due to different acceptances
 308 and to ensure a similar event structure, only tracks from events with similar vertex
 309 positions z ($|\Delta z| < 1 \text{ cm}$) and track multiplicities n ($|\Delta n| < 10$) were taken.

310 The mixed-event background distributions were normalised to two fixed regions,
 311 $1.49 < M_{\Xi\pi} < 1.51 \text{ GeV}/c^2$ and $1.56 < M_{\Xi\pi} < 1.58 \text{ GeV}/c^2$, around the Ξ^{*0} mass peak

(Fig. 5.1.4). These regions were used for all p_T intervals and multiplicity classes, because the background shape is reasonably well reproduced in these regions and the invariant-mass resolution of the reconstructed peaks appears stable, independently of p_T . The uncertainty on the normalisation was estimated by varying the normalisation regions and is included in the quoted systematic uncertainty for the signal extraction (Section 5.4).

After the background subtraction, the resulting distribution is shown in Figure 5.1.4. In order to obtain raw yields, a combined fit of a first-order polynomial for the residual background and a Voigtian function (a convolution of a Breit-Wigner and a Gaussian function accounting for the detector resolution) for the signal was used. The mathematical form of fit function used in analysis is:

$$f(M_{\Xi\pi}) = \frac{Y}{2\pi} \frac{\Gamma_0}{(M_{\Xi\pi} - M_0)^2 + \frac{\Gamma_0^2}{4}} \frac{e^{-(M_{\Xi\pi} - M_0)/2\sigma^2}}{\sigma\sqrt{2\pi}} + bg(M_{\Xi\pi}) \quad (1)$$

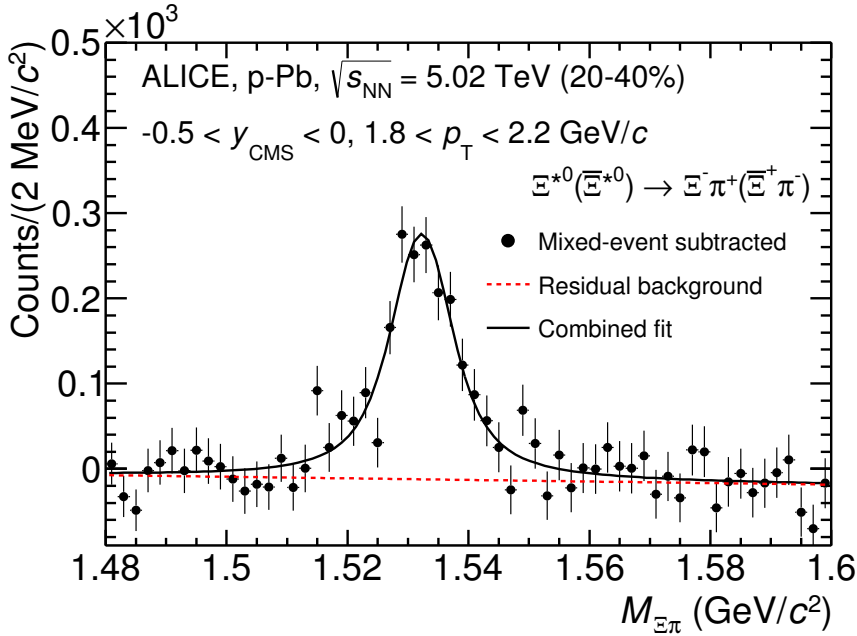


Figure 11: The invariant mass distribution after subtraction of the mixed-event background. The solid curve represents the combined fit, while the dashed line describes the residual background.

The mass parameter of the Voigtian fit (M_0) is left free within the fit range (1.48 GeV/ c^2 and 1.59 GeV/ c^2). The overall invariant mass width of the Voigtian function is governed by 2 parameters: σ and Γ_0 . The σ describes the broadening of the peak due

325 to finite detector resolution while Γ describes the intrinsic width of the resonance itself.
 326 The Γ_0 is fixed to the PDG value of 9.1 MeV/c for the $\Xi(1530)^0$. Due to lack of statistics in
 327 lowest p_T (0.8-1.4 GeV/c) and highest p_T (5.8-8.0 GeV/c) (specially in peripheral collision),
 328 the σ can be over estimated. Therefore the σ parameter is fixed to value derived from σ in
 329 MB events which has largest statistics. The σ as function of p_T distribution in MB events
 330 is shown in Figure. 12 and we also report invariant mass of $\Xi(1530)^0$ in Figure. 13.

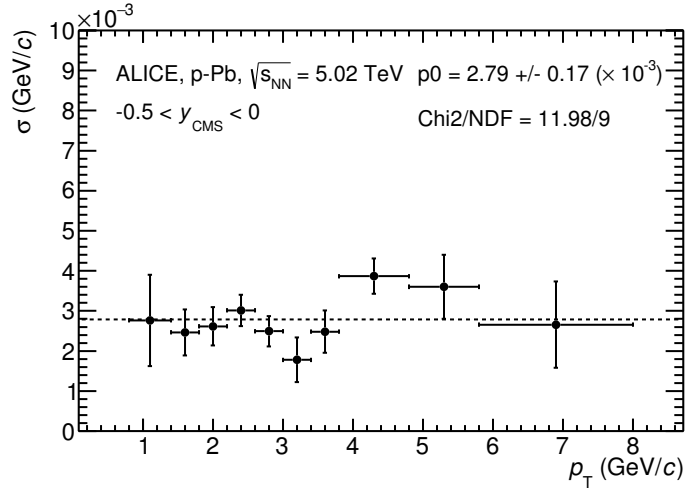


Figure 12: σ fit parameters as a function of p_T in MB.

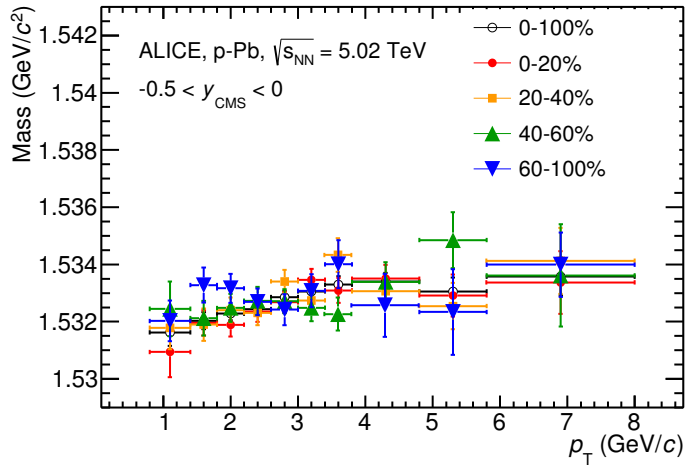


Figure 13: $\Xi(1530)^0$ -mass obtained from fit of the Voigtian peak as a function of p_T in each multiplicity classes.

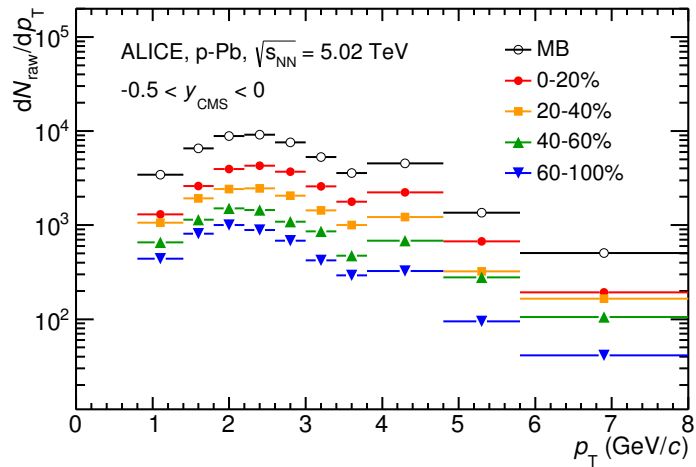


Figure 14: $\Xi(1530)^0$ -raw spectra obtained from fit of the Voigtian peak and a polynomial residual background for different multiplicities. Only the statistical error is reported.

331 **5.2 Efficiency correction**

332 The raw yields were corrected for the geometrical acceptance and the reconstruction effi-
 333 ciency ($A \times \epsilon$) of the detector (Figure. 15). By using the DPMJET 3.05 event generator [12]
 334 and the GEANT 3.21 package [13], a sample of about 100 million p-Pb events was sim-
 335 ulated and reconstructed in order to compute the corrections. The distributions of $A \times \epsilon$
 336 were obtained from the ratio between the number of reconstructed Ξ^{*0} and the number of
 337 generated particle in the same p_T and rapidity interval. Since the correction factors for
 338 different multiplicity classes are in agreement with those from MB events within statistical
 339 uncertainty, the latter were used for all multiplicity classes.

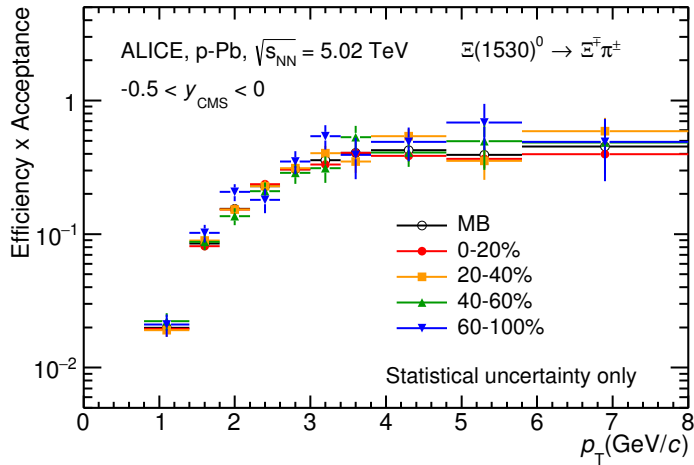


Figure 15: $\Xi(1530)^0$ -raw spectra obtained from fit of the Voigtian peak and a polynomial residual background for different multiplicities. Only the statistical error is reported.

340 Because the generated $\Xi(1530)^0$ spectra have different shapes than the measured $\Xi(1530)^0$ spectra,
 341 it is necessary to weight the generated and reconstructed $\Xi(1530)^0$ spectra in these sim-
 342 ulations. Fig. 16 shows the generated and reconstructed $\Xi(1530)^0$ spectra plotted with the
 343 (corrected) measured $\Xi(1530)^0$ spectrum for MB events and the Levy fit of that measured
 344 spectrum. The generated and measured $\Xi(1530)^0$ spectra have different behaviours for the
 345 range $0.5 < p_T < 1$ GeV/ c . The generated $\Xi(1530)^0$ spectrum decreases with increasing
 346 p_T over this range, while the fit of the measured $\Xi(1530)^0$ spectrum reaches a local max-
 347 imum in this range. The correction ϵ is observed to change rapidly over this p_T range.
 348 It is therefore necessary to weight the generated spectrum so that it has the shape of
 349 the measured $\Xi(1530)^0$ spectrum (and to apply corresponding weights to the reconstructed
 350 $\Xi(1530)^0$ spectrum). An iterative procedure is performed to determine the correct weighting
 351 (and therefore the correct ϵ).

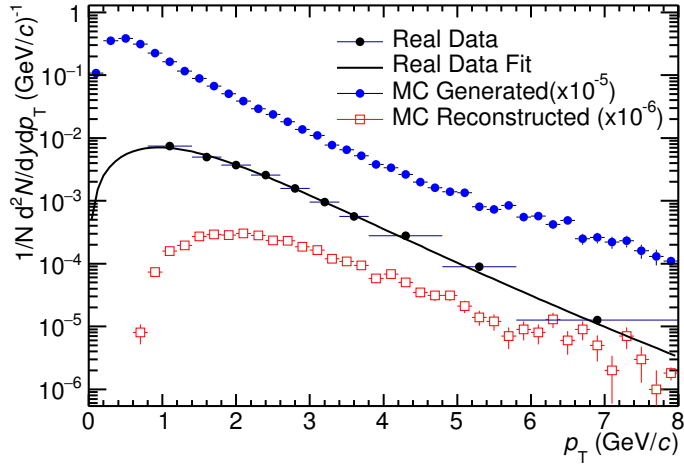


Figure 16: Real corrected $\Xi(1530)^0$ spectrum (black) for the minimum bias with Levy fit (black curve). Also shown are the unweighted generated (blue) and reconstructed (red) $\Xi(1530)^0$ spectra.

- 352 1. The unweighted ϵ is calculated.
 - 353 2. This ϵ is used to correct the measured xis spectrum.
 - 354 3. The corrected $\Xi(1530)^0$ spectrum is fit.
 - 355 4. This fit is used to weight the simulated xis spectra. A p_T dependent weight is applied
356 to the generated xis spectrum so that it follows the fit. The same weight is applied
357 to the reconstructedxis spectrum.
 - 358 5. The (weighted) ϵ is calculated.
 - 359 6. Steps 2-5 are repeated (with the weighted ϵ from step 5 used as the input for step 2)
360 until the ϵ values are observed to change by $< 0.1\%$ (relative) between iterations. It
361 is observed that four iterations are sufficient for this procedure to converge.
- 362 Finally, the re-weighted efficiency is obtained and the distribution as function of p_T is
363 shown in Figure 17.

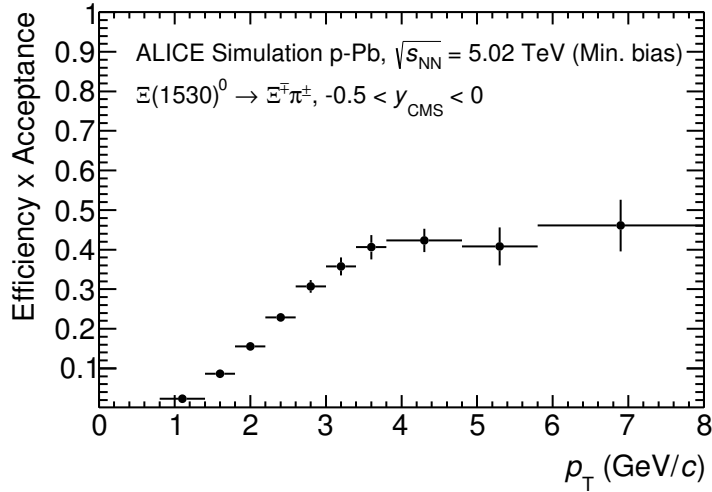


Figure 17: $\Xi(1530)^0$ -raw spectra obtained from fit of the Voigtian peak and a polynomial residual background for different multiplicities. Only the statistical error is reported.

364 **5.3 Corrected p_T -spectra**

365 The p_T spectrum is by the number of produced particles of a given type in the desired
 366 interval of phase-space divided by the number of inelastic collisions. The spectrum is
 367 calculated as:

$$\frac{1}{N} \times \frac{d^2N}{dydp_T} = \frac{1}{N_{E,PhysSel}} \times \frac{N_{raw}}{dp_T dy} \frac{1}{\epsilon} \frac{N_{total}^{MC}}{N_{post-PVcut}^{MC}}, \quad (2)$$

368 where N_E represent the number inelastic collisions, the $\frac{dN}{dydp_T}$ is the yield per range of
 369 rapidity y , per range in p_T . On the right hand side $N_{E,PhysSel}$ is the number of events
 370 counted by the PhysSelection trigger which is equal to the number of kINT7 triggers.
 371 N_{raw} is the raw extracted number of particle in the rapidity and p_T bin of width $\Delta y =$
 372 0.5 and Δp_T , respectively. ϵ is the reconstruction efficiency estimated from Monte Carlo
 373 simulations. $\frac{N_{total}^{MC}}{N_{post-PVcut}^{MC}}$ is the ratio of the total number of particle from MC divided by
 374 the number of particle from MC after the Primary-Vertex cut is imposed. It takes into
 375 account the fraction of particle lost after imposing the PV cut. For minimum-bias results
 376 we adopted a normalisation such that to provide result for p-Pb non-single diffractive(NSD)
 377 cross-section. The normalisation factor is 0.964 [6]. The obtained spectrum at MB and the
 378 spectrums from different multiplicity classes are shown in Fig. 18.

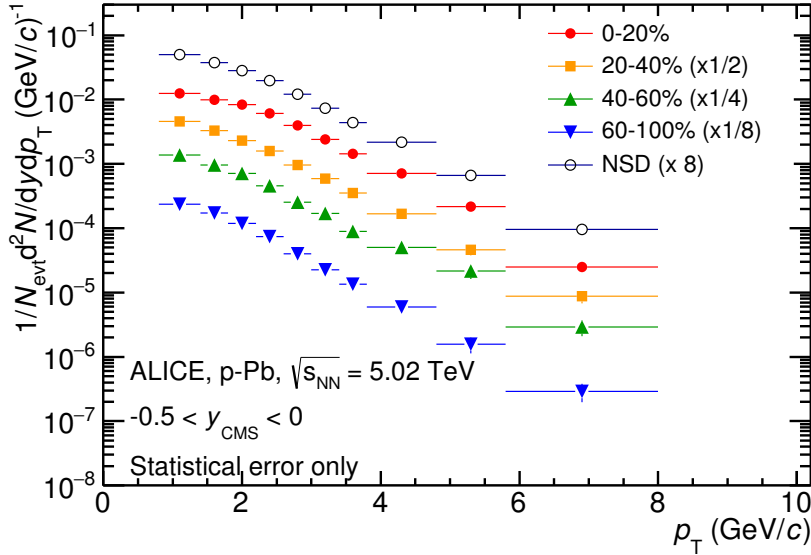


Figure 18: Corrected p_T -spectra of $\Xi(1530)^0$ in NSD and different multiplicity classes.

379 5.4 Systematic uncertainties

380 The systematic uncertainties are calculated in seven principle groups. The procedure to
 381 obtain the systematic uncertainties is performed many times by varying the possible per-
 382 mutation of the analysis parameter such as fit region, combinatorial background, PID cuts,
 383 etc. The general strategy for evaluating systematic uncertainties is described as following:

- 384 1. Choose one set of parameters for the analysis as default
- 385 2. Observe the deviation of yield when one parameter is changed
- 386 3. The systematic uncertainty is calculated for a given source as the RMS deviation of
 387 the available sources.
- 388 4. The total systematic uncertainty, taking into account all the different sources, is the
 389 sum in quadrature of each source.

390 To study the systematic effect we repeat the measurement by varying one parameter at
 391 a time. A Barlow [14] check has been performed for each measurement to verify whether it
 392 is due to a systematic effect or a statistical fluctuation. Let each measurement be indicated
 393 by $(y_i \pm \sigma_i)$ and the central value (default measurement) by $(y_c \pm \sigma_c)$, one can define $\Delta\sigma_i$
 394 (Eq. 3).

$$\Delta\sigma_i = \sqrt{(\sigma_i^2 - \sigma_c^2)} \quad (3)$$

395 Then we calculate $n_i = \Delta y_i / \Delta\sigma_i$, where $\Delta y_i = |y_c - y_i|$. If $n_i \leq 1.0$ then the effects
 396 are due to the statistical fluctuation and if $n_i > 1.0$ we apply consistency check. Since
 397 the alternate and default measurements are not statistically independent, an alternate
 398 measurement which is statistically consistent with the default measurement should not be
 399 used in calculating a systematic uncertainty. The difference between the two measurements
 400 is $\Delta = y_c - y_i$. The difference in quadrature of the uncertainties is calculated by Eq. 3. It
 401 could be possible to check if $\Delta < \sigma$ and exclude such cases from the systematic uncertainties.
 402 However, there can be statistical fluctuations for which $\Delta > \sigma$. If the variations between the
 403 default and alternate measurements are purely statistical, the distribution of Δ/σ should
 404 be a Gaussian with a mean value that is consistent with zero and a deviation σ consistent
 405 with unity. In this analysis, if the mean value is less than 0.1 and σ is less than 1, the
 406 variation passes the consistency check.

407 Only the measurements which passed the Barlow check ($n_i > 1$) are used to determine
 408 the systematic uncertainty. For measurements $N > 2$, the systematic uncertainty has been
 409 determined as the RMS (eqn. 4) of the available measurements. If $N=2$, the absolute
 410 difference is assigned as systematic uncertainty.

$$\delta y_{syst.} = \sqrt{\frac{1}{N} \sum_i (y_i - \bar{y})^2} \quad (4)$$

411 Here N is the total number of available measurements including y_c and \bar{y} is the average
 412 of value of the measurements. The measurement did not pass Barlow check, zero system-
 413 atic uncertainty has been assigned to the value.

414

415 5.4.1 Subgroup of systematic uncertainties

416 A. Systematic study: Signal extraction

417 The systematic uncertainty of yield extraction is estimated using three alternative methods.
 418 Default method of yield extraction corresponds to the bold letters.

- 419 1. Yield calculating method (U_{YC}) : **extract yield purely from a Voigtian fit** vs.
 420 bin-counting,
- 421 2. Background estimate method (U_{BE}) : **event mixing background** vs like-sign back-
 422 ground vs. polynomial fit(5^{th}).
- 423 3. Normalisation range (U_{NR}) : **1.49-1.51 , 1.56-1.58** vs. 1.48-1.51 , 1.56-1.58 (left
 424 extended) vs 1.49-1.51 , 1.56-1.59 (right extended).
 425 - The systematic uncertainty of the normalisation range is related to the invariant

426 mass region where the mixed events distribution is scaled to subtract the combina-
 427 torial background.

428 Total systematic uncertainty from signal extraction is the sum in quadrature of all the
 429 sources listed above.

$$U_{signal} = \sqrt{U_{YC}^2 + U_{BE}^2 + U_{NR}^2} \quad (5)$$

430 **B. Systematic study: Topological selection**

431 The analysis is performed by variations of the topological parameters with respect to
 432 the default values. The parameters are changed once at a time. Correlations between
 433 parameters are assumed to be negligible. The alternate sets of parameters are listed in
 434 Table 8.

Name		Loose	Standard	Tight	Name
DCA PV proton [cm]	>	0.05	0.06	0.07	U_{T1}
DCA PV last emitted π [cm]	>	0.05	0.06	0.07	U_{T2}
DCA PV second emitted π [cm]	>	0.01	0.0015	0.02	U_{T3}
DCA of Λ [cm]	>	0.01	0.015	0.02	U_{T4}
DCAz PV first emitted π [cm]	<	2.1	2.0	1.9	U_{T5}
DCA proton- π [cm]	<	1.5	1.4	1.3	U_{T6}
DCA Λ - π [cm]	<	2.0	1.9	1.8	U_{T7}
CPA Λ	>	0.85	0.875	0.9	U_{T8}
CPA Ξ^\pm	>	0.98	0.981	0.986	U_{T9}

Table 8: Alternate sets of topological parameters in the analysis.

435 Total systematic uncertainty from topological selection is calculated by same way which
 436 is done for systematic study of signal extraction.

$$U_{topological} = \sqrt{\sum_{i=1}^9 U_{Ti}^2} \quad (6)$$

437 **C. Systematic study: TPC $N_{cluster}$ selection**

438 The selection performed for the daughter tracks of the cascade is that $N_{cluster}$ is larger
 439 than 70 and the value has been varied to 60 and 80 in order to estimate the systematic
 440 uncertainty (U_{nCL}) due to this selection.

441 **D. Systematic study: TPC dE/dx selection**

442 In order to evaluate any potential effect due to the TPC dE/dx selection (U_{PID}), the N_σ
 443 selection was varied with $N = 2.5$ and 3.5 .

444 **F. Systematic study: Mass window range selection**

445 In order to select Ξ^\pm which is daughter particle of $\Xi(1530)^0$, we apply the mass window

⁴⁴⁶ $\pm 7 \text{ MeV}/c^2$ around $\Xi(1530)^0$ mass on $\Lambda\pi$ invariant mass distribution. The boundaries has
⁴⁴⁷ been varied to $\pm 6 \text{ MeV}/c^2$ and $\pm 8 \text{ MeV}/c^2$ to estimate systematic uncertainty (U_{MW}).

G. Systematic study: Vertex range selection

⁴⁴⁹ The distribution of vertex-z is shown in Fig.3. The cut on $|Vz|$ was varied from the nominal
⁴⁵⁰ $\pm 10\text{cm}$ to $\pm 9\text{cm}$, $\pm 11\text{cm}$.

451 5.4.2 Summary of systematic uncertainties

⁴⁵² Final statistical uncertainty from all sources is defined as sum in quadrature (Eq. 7).

$$U_{total} = \sqrt{U_{signal}^2 + U_{topological}^2 + U_{nCL}^2 + U_{PID}^2 + U_{MW}^2 + U_{Vz}^2 + U_{MB}^2 + U_{TE}^2} \quad (7)$$

⁴⁵³ Fig.19 and Fig.20 show the total systematic uncertainty.

⁴⁵⁴ In the eq. 7, U_{MB} is uncertainty due to material budget which is 4% from Ξ^\pm and
⁴⁵⁵ material budget from π is negligible. The U_{TE} is uncertainty due to tracking efficiency
⁴⁵⁶ which amount is 3%.

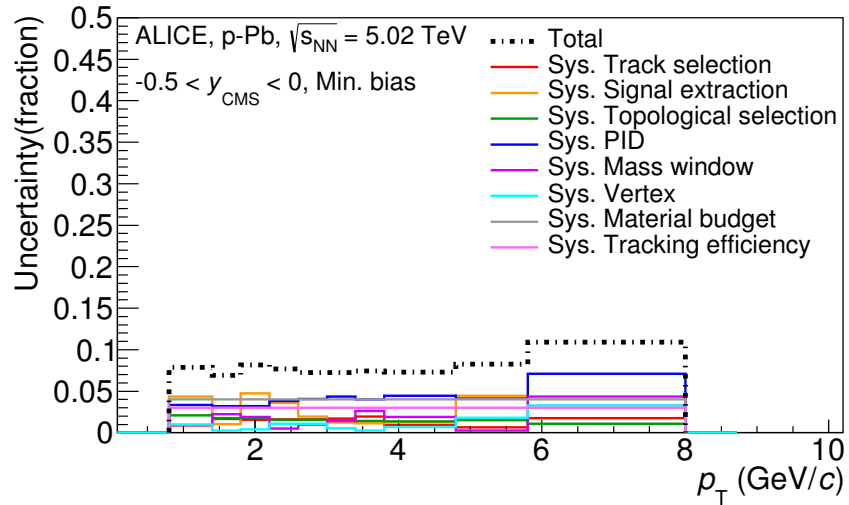


Figure 19: Summary of the contributions to the systematic uncertainty after consistency check in MB. The dashed black line is the sum in quadrature of all the contributions.

457 Smoothing of systematic error

⁴⁵⁸ One should expect a smooth behaviour of the systematic uncertainties. But in data we
⁴⁵⁹ observed some of the raw systematic uncertainties fluctuate from bin to bin. So we need
⁴⁶⁰ to smooth the spikes and dips in the systematic uncertainties. We compare the systematic

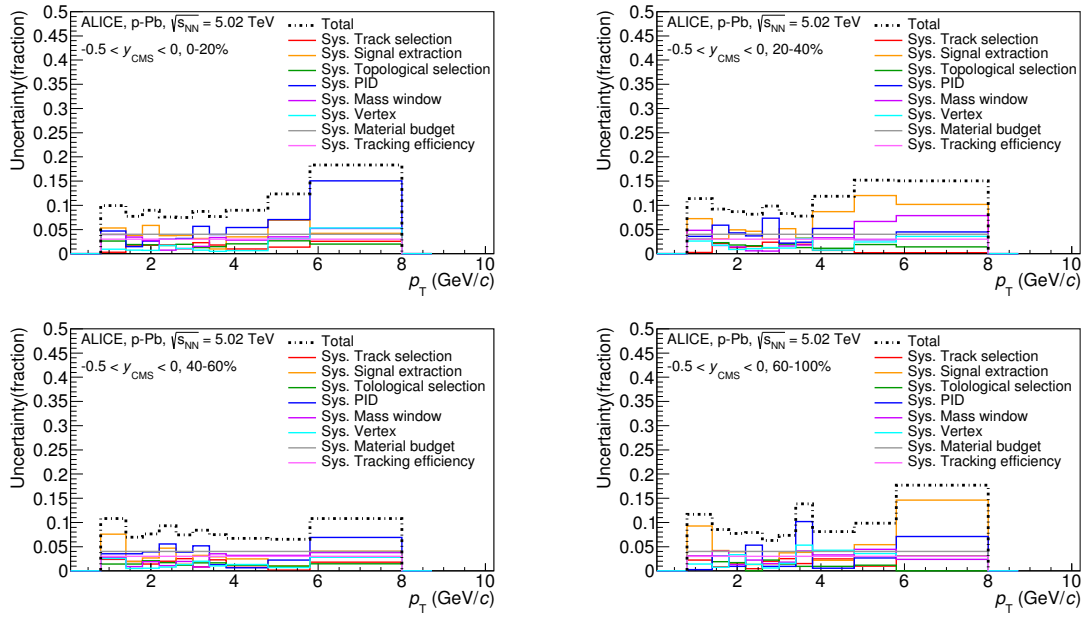


Figure 20: Summary of the contributions to the systematic uncertainty after consistency check for each multiplicity class(0-20-40-60-100). The dashed black line is the sum in quadrature of all the contributions.

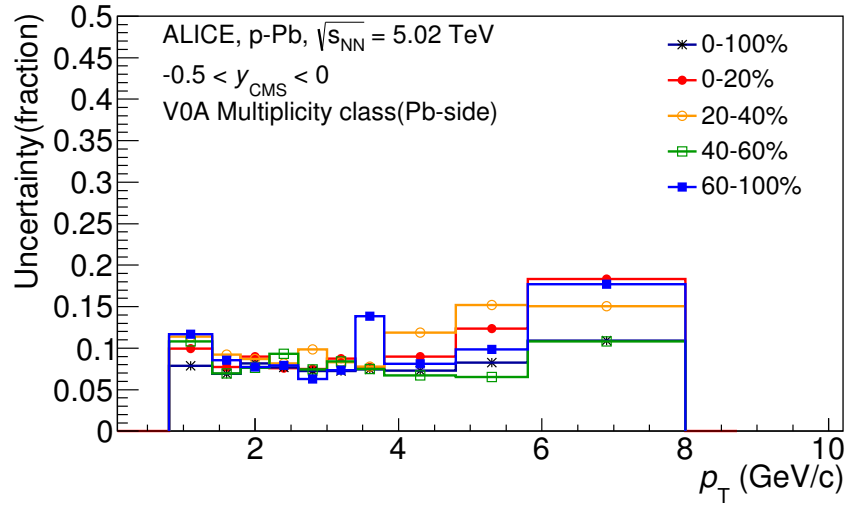


Figure 21: Fractional systematic uncertainties for each multiplicity classes.

461 uncertainty of the problematic p_T bins to the values from the other centrality class system-
 462 atic uncertainty which gives us an idea of the value for the bin. Average values considering
 463 all centrality classes are calculated for each p_T bins and the average value is written in Table
 464 21. If the value of error is larger than of average $\times 1.1$, the average value is applied for the
 465 error. The smoothed systematic uncertainties for all centrality classes and minimum-bias
 466 are shown in Fig.22.

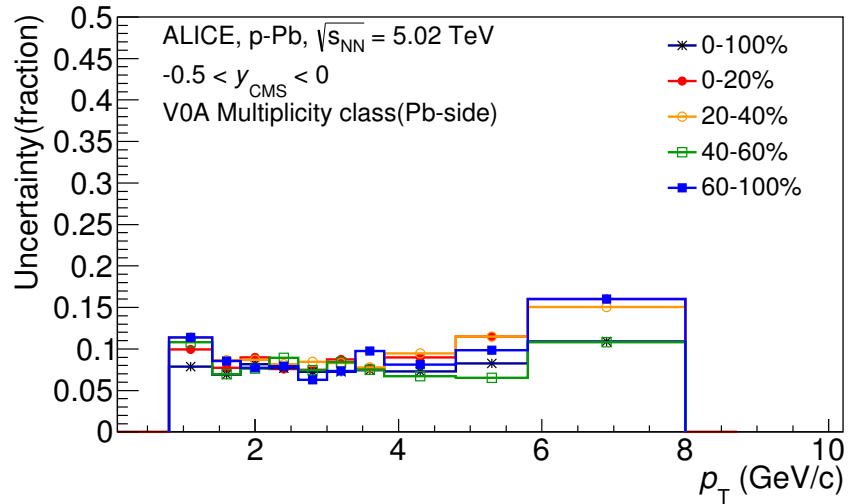


Figure 22: Fractional smoothed systematic uncertainties for each multiplicity classes.

467 **5.5 $\Xi(1530)^0$ transverse momentum spectra**

468 The corrected yields per p_T interval per unit rapidity ($\frac{1}{N_E} \times \frac{d^2N}{dydp_T}$) are shown in Fig.23.
 469 Data points cover the p_T ranges $0.8 < p_T < 8.0$ GeV/ c . Statistical and systematical uncer-
 470 tainties are plotted separately.

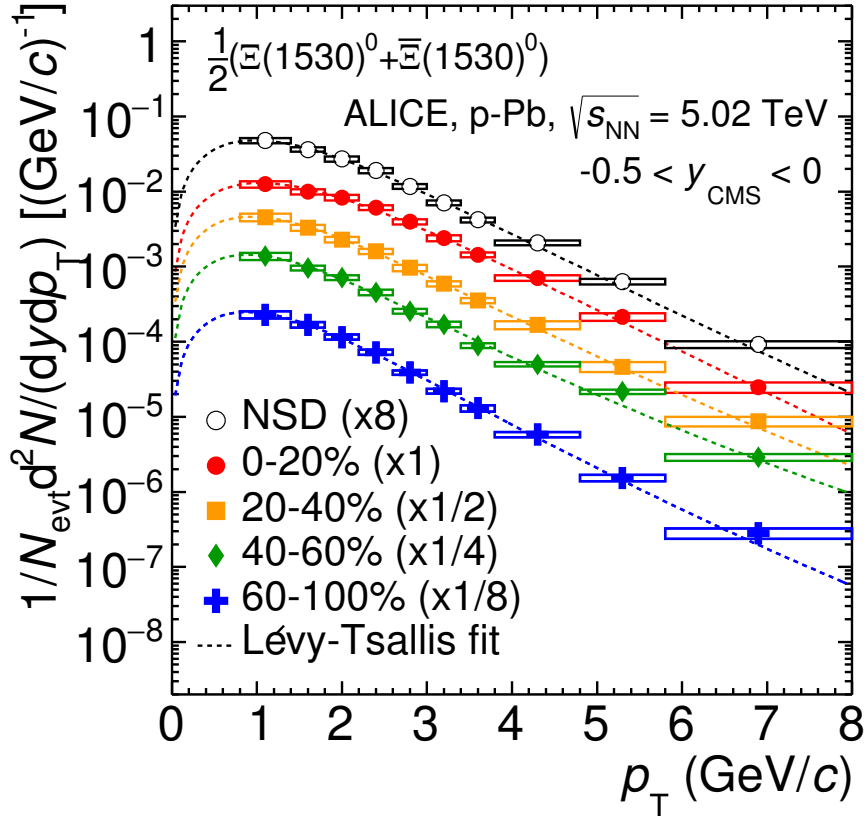


Figure 23: Corrected yields as function of p_T in NSD events and multiplicity dependent event classes. Statistical uncertainties are presented as bar and systematical uncertainties are plotted as boxes.

471 **6 Measurement of $\Xi(1530)^0$ production in Pb–Pb**

472 The measurement of resonance production in ultra-relativistic heavy-ion collisions provides
 473 information on the properties of the hadronic medium and different stages of its evolution.

474 The measurement of the short-lived resonances allows to estimate the time span in the
475 hadronic phase between the chemical and the kinetic freeze-out. In order to study the
476 particle production mechanism, the $\Xi(1530)^0$ resonance production at mid-rapidity is mea-
477 sured in p–Pb collisions $\sqrt{s_{\text{NN}}}= 5.02$ TeV and in Pb–Pb collisions at $\sqrt{s_{\text{NN}}}= 2.76$ TeV with
478 the ALICE experiment, via the reconstruction of its hadronic decay into $\Xi\pi$.

479 **6.1 $\Xi(1530)^0$ -reconstruction**

480 The Ξ^* production in p–Pb collisions at $\sqrt{s_{\text{NN}}}= 5.02$ TeV and Pb–Pb interactions at
481 $\sqrt{s_{\text{NN}}}= 2.76$ TeV at mid-rapidity has been studied in different multiplicity(p–Pb) and
482 centrality(Pb–Pb) classes, from very central to peripheral collisions. The analysis strategy
483 is based on the invariant mass study of the reconstructed pairs (referred to as the candi-
484 dates) whose provenance could be the decay of a Ξ^* baryon into charged particles. The decay products (also called daughters in the text) are identified as oppositely charged Ξ and
485 π among the tracks reconstructed in the central barrel. The event selection, track selec-
486 tion and the particle identification strategy is described. The raw signal yield is extracted
487 by fitting the background-subtracted invariant mass distribution in several transverse mo-
488 mentum intervals. In order to extract the p_{T} -dependent cross section, these yields are
489 corrected for efficiency. The p_{T} -dependent correction due to the detector acceptance and
490 reconstruction efficiency, $(\text{Acc} \times \epsilon_{\text{rec}})(\text{pt})$, is computed from a Monte Carlo simulation.
491 The absolute normalisation is then performed, by dividing for the number of the events in
492 each multiplicity/centrality classes.

494 **6.1.1 Data sample and event selection**

495 The data used in this note come from p–Pb, $\sqrt{s_{\text{NN}}}= 5.02$ TeV collisions measured by the
496 ALICE experiment during the 2013 run at the LHC. About 111.1×10^6 minimum bias(MB)
497 events are selected as data sample which was obtained with AND logic of V0A and V0C.

498 As event selection for data sample in Pb–Pb collisions, three different trigger selections(kCentral(0-
499 10%), kSemiCentral(10-50%) and kMB(0-90%)) are applied and corresponding number of
500 events are 24.8 M events in central event, 21.8 M events in semi-central events and 3.5 M
501 events in minimum-bias events.

- 502 **6.1.2 Topological selection**
- 503 **6.1.3 Particle identification**
- 504 **6.2 Efficiency correction**
- 505 **6.3 Systematic uncertainties**
- 506 **6.4 $\Xi(1530)^0$ transverse momentum spectra**

507 **7 Results**

- 508 **7.1 dN/dy and $\langle p_T \rangle$**
- 509 **7.2 Particle yield ratios**
- 510 **7.2.1 Comparison with other resonances**
- 511 **7.2.2 Comparison with models**

512 **References**

- 513 [1] D. Hahn and H. Stoecker, “THE QUANTUM STATISTICAL MODEL OF
514 FRAGMENT FORMATION: ENTROPY AND TEMPERATURE EXTRACTION
515 IN HEAVY ION COLLISIONS,” *Nucl. Phys.* **A476** (1988) 718–772.
- 516 [2] S. Wheaton, J. Cleymans, and M. Hauer, “THERMUS: A Thermal model package
517 for ROOT,” *Comput. Phys. Commun.* **180** (2009) 84–106, [hep-ph/0407174](#).
- 518 [3] J. Cleymans, S. Kabana, I. Kraus, H. Oeschler, K. Redlich, and N. Sharma,
519 “Antimatter production in proton-proton and heavy-ion collisions at ultrarelativistic
520 energies,” *Phys. Rev.* **C84** (2011) 054916, [arXiv:1105.3719 \[hep-ph\]](#).
- 521 [4] **ALICE** Collaboration, K. Aamodt *et al.*, “The ALICE experiment at the CERN
522 LHC,” *JINST* **3** (2008) S08002.
- 523 [5] **ALICE** Collaboration, B. Abelev *et al.*, “Performance of the ALICE Experiment at
524 the CERN LHC,” *Int. J. Mod. Phys.* **A29** (2014) 1430044, [arXiv:1402.4476](#)
525 [nucl-ex].
- 526 [6] **ALICE** Collaboration, J. Adam *et al.*, “Production of $K^*(892)^0$ and $\phi(1020)$ in
527 p–Pb collisions at $\sqrt{s_{NN}} = 5.02$ TeV,” *Eur. Phys. J.* **C76** (2016) 245,
528 [arXiv:1601.7868 \[nucl-ex\]](#).
- 529 [7] **ALICE** Collaboration, B. Abelev *et al.*, “Pseudorapidity Density of Charged
530 Particles in p–Pb Collisions at $\sqrt{s_{NN}} = 5.02$ TeV,” *Phys. Rev. Lett.* **110** (2013)
531 032301, [arXiv:1210.3615 \[nucl-ex\]](#).

- 532 [8] **ALICE** Collaboration, B. Abelev *et al.*, “Production of $\Sigma(1385)^{\pm}$ and $\Xi(1530)^0$ in
533 proton-proton collisions at $\sqrt{s}= 7$ TeV,” *Eur. Phys. J.* **C75** (2015) 1,
534 arXiv:1406.3206 [nucl-ex].
- 535 [9] **Particle Data Group** Collaboration, K. Olive *et al.*, “Review of Particle Physics,”
536 *Chin. Phys.* **C38** (2014) 090001.
- 537 [10] **ALICE** Collaboration, J. Adam *et al.*, “Multi-strange baryon production in p–Pb
538 collisions at $\sqrt{s_{\text{NN}}}=5.02$ TeV,” *Phys. Lett.* **B758** (2016) 389–401,
539 arXiv:1512.07227 [nucl-ex].
- 540 [11] **ALICE** Collaboration, K. Aamodt *et al.*, “Strange particle production in
541 proton-proton collisions at $\sqrt{s}= 0.9$ TeV with ALICE at the LHC,” *Eur. Phys. J.*
542 **C71** (2011) 1594, arXiv:1012.3257 [nucl-ex].
- 543 [12] S. Roesler, R. Engel, , and J. Ranft, “The Monte Carlo Event Generator
544 DPMJET-III, Advanced Monte Carlo for Radiation Physics, Particle Transport
545 Simulation and Applications,” *Conference Proceedings, MC2000, Lisbon, Portugal,*
546 *October 23-26* (2000) 1033–1038, hep-ph/0012252.
- 547 [13] R. Brun, F. Carminati, and S. Giani, “GEANT detector description and simulation
548 tool,” *CERN-W5013* (1994) .
- 549 [14] R. Barlow, “Systematic Errors: Facts and Fictions,” *Presented at Advanced*
550 *Statistical Techniques in HEP, Durham, March 2002* (2002) 333p,
551 hep-ex/0207026v1.

552 **Acknowledgements**